NASA/ TM-20260005710

Fatigue Behavior Of Laser Powder Bed Fused HAYNES 214: Effects Of Different Surface Treatments

Erfan Maleki
National Center for Additive Manufacturing Excellence (NCAME), Auburn, AL
Department of Mechanical Engineering, Auburn Univeristy, Auburn, AL

Shaikha Shohuda Tuktuk
National Center for Additive Manufacturing Excellence (NCAME), Auburn, AL
Department of Mechanical Engineering, Auburn Univeristy, Auburn, AL

Colton Katsarelis
NASA Marshall Space Flight Center, Huntsville, AL

Paul R. Gradl
NASA Marshall Space Flight Center, Huntsville, AL

Shuai Shao
National Center for Additive Manufacturing Excellence (NCAME), Auburn, AL
Department of Mechanical Engineering, Auburn Univeristy, Auburn, AL

Nima Shamsaei
National Center for Additive Manufacturing Excellence (NCAME), Auburn, AL
Department of Mechanical Engineering, Auburn Univeristy, Auburn, AL

August 2026

NASA STI Program Report Series

Since its founding, NASA has been dedicated to the advancement of aeronautics and space science. The NASA scientific and technical information (STI) program plays a key part in helping NASA maintain this important role.

The NASA STI program operates under the auspices of the Agency Chief Information Officer. It collects, organizes, provides for archiving, and disseminates NASA's STI. The NASA STI program provides access to the NTRS Registered and its public interface, the NASA Technical Reports Server, thus providing one of the largest collections of aeronautical and space science STI in the world. Results are published in both non-NASA channels and by NASA in the NASA STI Report Series, which includes the following report types:

- TECHNICAL PUBLICATION. Reports of completed research or a major significant phase of research that present the results of NASA Programs and include extensive data or theoretical analysis. Includes compilations of significant scientific and technical data and information deemed to be of continuing reference value. NASA counterpart of peer-reviewed formal professional papers but has less stringent limitations on manuscript length and extent of graphic presentations.

- TECHNICAL MEMORANDUM. Scientific and technical findings that are preliminary or of specialized interest, e.g., quick release reports, working papers, and bibliographies that contain minimal annotation. Does not contain extensive analysis.

- CONTRACTOR REPORT. Scientific and technical findings by NASA-sponsored contractors and grantees.

- CONFERENCE PUBLICATION. Collected papers from scientific and technical conferences, symposia, seminars, or other meetings sponsored or co-sponsored by NASA.

- SPECIAL PUBLICATION. Scientific, technical, or historical information from NASA programs, projects, and missions, often concerned with subjects having substantial public interest.

- TECHNICAL TRANSLATION. English-language translations of foreign scientific and technical material pertinent to NASA's mission.

Specialized services also include organizing and publishing research results, distributing specialized research announcements and feeds, providing information desk and personal search support, and enabling data exchange services.

For more information about the NASA STI program, see the following:

- Access the NASA STI program home page at http://www.sti.nasa.gov

.

NASA/ TM-20260005710

Fatigue Behavior Of Laser Powder Bed Fused HAYNES 214: Effects Of Different Surface Treatments

Erfan Maleki
National Center for Additive Manufacturing Excellence (NCAME), Auburn, AL
Department of Mechanical Engineering, Auburn Univeristy, Auburn, AL

Shaikha Shohuda Tuktuk
National Center for Additive Manufacturing Excellence (NCAME), Auburn, AL
Department of Mechanical Engineering, Auburn Univeristy, Auburn, AL

Colton Katsarelis
NASA Marshall Space Flight Center, Huntsville, AL

Paul R. Gradl
NASA Marshall Space Flight Center, Huntsville, AL

Shuai Shao
National Center for Additive Manufacturing Excellence (NCAME), Auburn, AL
Department of Mechanical Engineering, Auburn Univeristy, Auburn, AL

Nima Shamsaei
National Center for Additive Manufacturing Excellence (NCAME), Auburn, AL
Department of Mechanical Engineering, Auburn Univeristy, Auburn, AL

National Aeronautics and
Space Administration

Marshall Space Flight Center
Huntsville, AL

August 2026

National Aeronautics and
Space Administration

Marshall Space Flight Center
Huntsville, AL

August 2026

Available from:

NASA STI Program / Mail Stop 050
NASA Langley Research Center
Hampton, VA 23681-2199

Author's Note

This research is partially supported by the National Aeronautics and Space Administration (NASA) under contract No. 80MSFC19C0010. This paper describes objective technical results and analysis. Any subjective views or opinions that might be expressed in the paper do not necessarily represent the views of NASA or the United States Government.

Table of Contents

Table of Contents 2
List of Figures 3
List of Tables 4
List of Acronyms and Abbreviations 5
Nomenclature 6
1.0 Introduction 7
2.0 Experimental Procedure 9
2.1 Fabrication and Processing Conditions 9
2.2 Surace Post-Treatments 10
2.3 Surface Characterization 11
2.4 Microstructural Characterization 11
2.5 Fatigue Testing 11
3.0 RESULTS AND DISCUSSIONS 12
3.1 Surface Texture 12
3.2 Microstructure 16
3.3 Fatigue Behavior 17
4.0 CONCLUSIONS 23
Appendix A 24
Appendix B 25
References 27

List of Figures

Figure 1. (a) Fatigue test specimens' design with corresponding geometry and dimensions, and (b) thermal post-processing steps, including SR, HIP, and ST. 9

Figure 2. (a) Surface appearance of the specimens taken with camera, as well as surface textures in all conditions at different magnifications captured by (b) optical microscope and (c) SEM. .. 13

Figure 3. (a) 3D surface topography maps of all conditions obtained within a 2 × 2 mm² area. Surface roughness values in terms of (b) S_a, (c) S_v, (d) S_p, (e) S_z, (f) S_k and (g) S_{vk} parameters for all sets. (h) Comparison of efficiency of applied SPTs for surface texture modification compared to the as-built surface considering all roughness parameters. 15

Figure 4. IPF and Kam maps of the microstructural characterization results obtained from EBSD for all conditions. 17

Figure 5. The results of strain-life fatigue tests for all conditions at (a) four different strain amplitudes and separately for strain amplitudes of (b) 0.0025 mm/mm, (c) 0.003 mm/mm, (d) 0.004 mm/mm, and (f) 0.005 mm/mm. 20

Figure 6. SEM fracture surfaces of failed specimens tested at strain amplitude of (a) ε_a = 0.0025 mm/mm and (b) ε_a = 0.004 and 0.005 mm/mm. In addition, red and green arrows demonstrate surface crack initiation and remained surface valleys, respectively. 22

Figure 7. Comparison of the distribution of volumetric defects in as-built state and after applying HT+HP. .... **Error! Bookmark not defined.**

Figure 8. The hysteresis loops corresponding to different strain amplitudes demonstrating elastic and plastic regimes in the untreated and treated conditions. 24

List of Tables

Table 1. Chemical composition of Alloy 214 powder. 9

Table 2. A summary of strain-life fatigue results for various surface conditions at $R_\varepsilon = -1$. 25

List of Acronyms and Abbreviations

AFM	Abrasive Flow Machining
CM	Chemical Milling
CMP	Chemical Mechanical Polishing
DE	Dry Electropolishing
EBSD	Electron Backscatter Diffraction
ECP	Electro-Chemical Polishing
HIP	Hot Isostatic Pressing
IPF	Inverse Pole Figure
KAM	Kernel Average Misorientation
LP	Laser Polishing
L-PBF	Laser Powder Bed Fused
M	Machining
psi	Pounds Per Square Inch
RAMPT	Rapid And Analysis Manufacturing Propulsion Technology
SEM	Scanning Electron Microscopy
SP	Shot Peening
SPT	Surface Post Treatments
SR	Stress Relief
ST	Solution Treatment
UT	Untreated
VM	Vapormatt
XCT	X-Ray Computed Tomography

Nomenclature

R_a/S_a	Average Roughness of the Profile Line/Surface
S_v	Maximum Valley Depth
S_z	Maximum Height
S_p	Maximum Peak Height
S_k	Core Roughness Depth
S_{vk}	Reduced Valley Depth
R_ε	Strain Ratio
ε_a	Strain Amplitude
$2N_f$	Reversals To Failure

1.0 INTRODUCTION

Nickel-base superalloys represent the predominant class of high-temperature metallic alloys, particularly suited for applications that require reliable performance under extreme temperature and stress conditions [1–6]. HAYNES 214 (Alloy 214) is an austenitic nickel-base superalloy engineered to endure oxidative environments at temperatures above 1000 °C and under high pressure conditions up to 10000 psi. The applications of this alloy encompass gas turbine components such as honeycomb seals and combustor parts, industrial heating equipment parts like refractory anchors and fixtures in furnaces, and catalytic converter internals [7–12]. Specifically, Alloy 214 offers significant advantages in high-pressure and high-temperature oxygen environments such as those encountered rocket engines [13,14]. However, fabrication of parts/components with Alloy 214 has proven to be challenging due to geometrical complexity when using conventional manufacturing methods, such as subtractive processes [15]. Considering this challenge, additive manufacturing (AM) processes such as laser powder bed fusion (L-PBF) can be considered as acceptable alternatives for fabrication of complex geometries with nickel-base superalloys [16–21]. Beside numerous advantages of L-PBF (such as design freedom, customization, intricate geometries, rapid prototyping, and reduced material waste), the parts fabricated by this technique in their as-built state exhibit various volumetric defects and surface anomalies (unmelted and partially melted powders, spatters and surface valleys), which adversely affect their mechanical performance [22–26].

There are numerous studies in the literature on the effects of post-processing methods including heat treatment (HT) and hot isostatic pressing (HIP) applied to L-PBF fabricated nickel-base superalloys, including IN718 [27–29], IN625 [30–32], HAYNES 282 [33–35], and Alloy 214 [7,36]. However, regarding application of surface enhancement by surface post-treatments (SPTs), only a few studies have been carried out on L-PBF fabricated nickel-base superalloys [37,38]. Lee et al. [39] investigated the effects of different SPTs of sand blasting, drag finishing, turning, and grinding on the surface texture and fatigue behavior of L-PBF fabricated IN 718. The results revealed that the arithmetic average roughness (R_a) of 4.35 µm in as-built state was considerably diminished to 3.14, 2.71, 1.08, and 0.37 after applying sand blasting, drag finishing, turning, and grinding, respectively. Accordingly, all SPTs led to enhancement in fatigue resistance with G causing the most improvement. In another study, Jiang et al. [40] surveyed the effect of electro-chemical polishing (ECP) on the surface texture of L-PBF fabricated Hastelloy X. It was reported that the surface roughness for the as-built condition, approximately 10.23 µm in terms of Ra_a, was reduced to about 7.3, 4.7, 4.1, 3.4, and 1.9 µm after applying ECP with a mixture of choline chloride and ethylene etchant for 1, 2, 3, 4, and 5 minutes, respectively. In the study performed by Ahmad et al., influences of various SPTs including abrasive flow machining (AFM), machining (M), shot peening (SP), vapormatt (VM), dry electropolishing (DE), chemical milling (CM), chemical-mechanical polishing (CMP), ECP, and laser polishing (LP) on variations of surface quality as well as fatigue behavior of L-PBF HAYNES 282 were investigated. The results indicated that surface roughness of as-built condition with about 6.2 µm in terms of areal arithmetical mean height (S_a) decreased down to 5.1, 5, 2.2, 4.6, 0.3, 0.6, and 0.5 after performing SP, VM, DE, CMP, ECP, AFM, and LP treatments respectively. In addition, notable improvement in fatigue lives at lower strain amplitudes ≤0.003 mm/mm was obtained after applying mechanical surface treatments. It should be noted that, to the best of the authors' knowledge, this is the first paper to study the effects of various SPTs on the fatigue behavior of L-PBF Alloy 214.

In this study, under NASA's Rapid and Analysis Manufacturing Propulsion Technology (RAMPT) project [41], effects of different SPTs on surface texture and fatigue behavior of L-PBF Alloy 214 were investigated. Various subtractive SPTs including CM, DE, AFM, ECP, CMP, and M were applied to study the variations of the surface texture, microstructure and uniaxial fatigue behavior under fully reversed strain-controlled condition at four different strain amplitudes of 0.005, 0.004, 0.003, and 0.0025 mm/mm. The insights gained regarding the relationship between structural and mechanical properties for different SPTs can help establish guidelines for selecting the most effective process to enhance the performance of L-PBF Alloy 214, especially for critical aerospace applications.

2.0 EXPERIMENTAL PROCEDURE

2.1 Fabrication and Processing Conditions

Cylindrical specimens were fabricated using Praxair TruForm Alloy 214 powder, with an average particle size of 43.1 µm (D10 = 18.2 µm, D50 = 30.2 µm, and D90 = 48.1 µm). The powder's chemical composition is presented in Table 1. The specimens were produced in a vertical orientation in accordance with the ASTM E606 [42] for strain-controlled fatigue testing. The specimens were manufactured using an EOS M400–4 system with laser power set at 200 W, scanning speed of 1000 mm/s, and layer thickness of 40 µm. Design geometry and dimensions of fatigue test specimens are shown in Figure 1(a).

Table 1. Chemical composition of Alloy 214 powder.

Element	Ni	Cr	Al	Fe	Co	Si	Mn	O	C	Y	S	B	P
Wt. (%)	Bal.	15.79	4.19	2.48	0.12	0.04	0.02	0.02	0.01	0.01	0.001	<0.001	<0.005

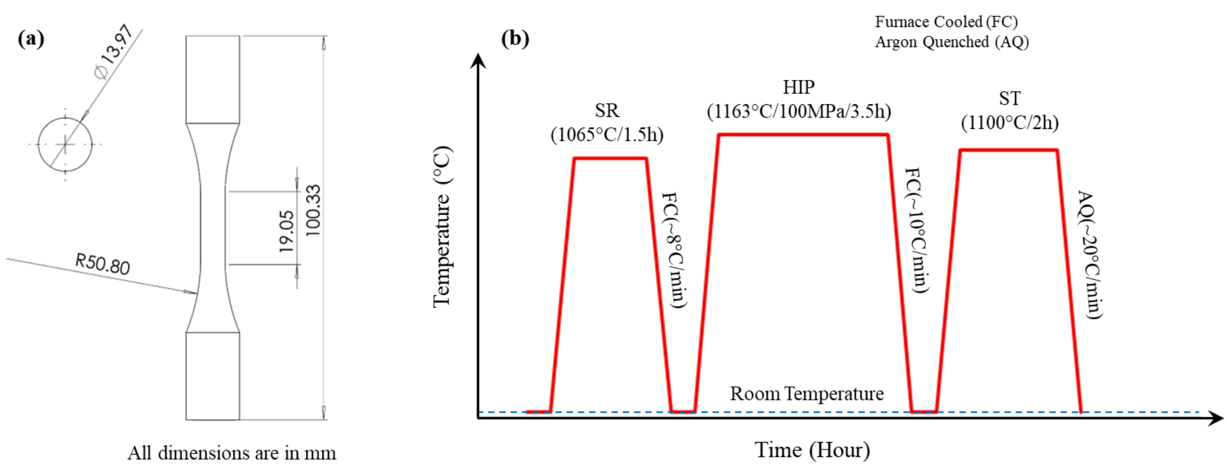

Figure 1. (a) Fatigue test specimens' design with corresponding geometry and dimensions, and (b) thermal post-processing steps, including SR, HIP, and ST.

After the fatigue specimens were removed from the build plate, they underwent a standard heat treatment [43], including stress relief (SR), HIP and solution treatment (ST) as shown in Figure 1(b). SR was conducted at 1065 °C for 1.5 hours and furnace cooled (FC) at the rate of 8 °C/min. Following that, the specimens went through HIP at 1163°C and 100 MPa pressure for 3.5 hours and FC at 10°C/min. Finally, ST was completed at 1100°C for 2 hours and rapidly argon quenched (AQ) at the rate of 20°C/min. It should be noted that X-ray computed tomography (XCT) was used for specimens' gages defect analysis and porosity measurement after applying HT and HIP. The analysis revealed no volumetric defects in the scanned volume (as depicted in Figure 2).

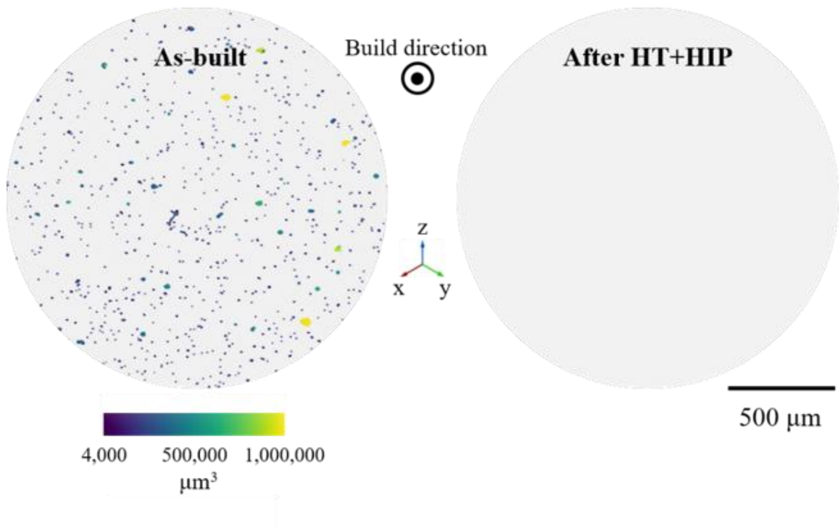

Figure 2. Comparison of the distribution of volumetric defects in as-built state and after applying HT+HP.

2.2 Surace Post-Treatments

Different subtractive SPTs including CM, DE, AFM, ECP, CMP, and M were applied on the specimens, and a total of seven conditions were considered with untreated as-built condition (UT) state as baseline. CM uses baths of temperature-regulated etching chemicals to remove surface material and form new surface patterns [44]. DE is an electrochemical surface finishing technique that removes microscale peaks from metal surfaces by solid electrolyte beads instead of liquid baths [45]. ECP is a reverse electroplating process that uses an electric current in an electrolyte to dissolve metal from the surface of a workpiece, eliminating surface anomalies/imperfections to achieve a smooth finish. This method is particularly suitable for intricate shapes or complex components where mechanical polishing poses challenges [46]. CMP, often referred to as tumble finishing, is an economical method that concurrently polishes, deburrs, and smoothens a large number of parts by tumbling them in a barrel filled with abrasive media, and chemical agents to generate friction and then produce a smooth surface [47]. AFM is a surface finishing technique that uses a high pressure viscous medium back and forth through the workpiece to planarize, deburr, and polish rough surfaces or, more often, interior surfaces or difficult-to-reach places [48]. It should be noted that for the specimens subjected to SPTs, oversized specimens with radius increase of 0.5 mm were used, necessitating material removal without changes to the size of the specimens.

2.3 Surface Characterization

To characterize surface texture, an optical microscope, Keyence VK-X1000, was used. The instrument operates on focus variation method and a pixel size of 1.3 µm was utilized for this analysis. Prior to surface characterization, the specimens were cleaned and sonicated using isopropanol. Different surface roughness parameters including arithmetical Mean Height (S_a), Maximum Valley Depth (S_v), Maximum Height (S_z), Maximum Peak Height (S_p), areal functional parameters including core roughness depth (S_k), and reduced valley depth (S_{vk}), were evaluated according to ISO 25178–2:2021 standard [49], using a Gaussian S-filter with a cutoff wavelength (λc) of 0.8 mm. In addition, surface morphologies were observed by scanning electron microscopy (SEM) using a Zeiss Crossbeam 550 microscope.

2.4 Microstructural Characterization

Near surface microstructural characterization was performed using a Zeiss Crossbeam 550 scanning electron microscope equipped with electron backscatter diffraction (EBSD). Specimens were sectioned perpendicular to the build direction, mounted and polished using sandpapers with grit size ranging from 240 to 1000 as well as ChemoMet and vibratory polisher for fine polishing. At 20 kV voltage and 3 nA current, EBSD analysis was conducted using a working distance lower than 15 mm. The mounted samples were tilted at 70 degrees. Before performing fractography, the fracture surfaces were cut, cleaned, and sonicated with isopropanol.

2.5 Fatigue Testing

Following ASTM E606 standard [42], fully reversed ($R_\varepsilon = -1$), uniaxial, strain-controlled fatigue tests were conducted using a triangular waveform on a servo-hydraulic MTS fatigue machine. Specimens were tested at four different strain amplitudes: 0.0025, 0.003, 0.004, and 0.005 mm/mm. At each strain amplitude and each surface treatment condition, three specimens were tested. All of the fatigue tests were carried out by IMR Test Labs.

3.0 RESULTS AND DISCUSSIONS

3.1 Surface Texture

In Figure , the surface morphologies of specimens after applying different SPTs along with UT state are depicted, as taken by a camera (Figure (a)), optical microscope (Figure (b)), and SEM (Figure (c)) at various magnification scales. The UT as-built surface condition contains spatters, partially melted and unmelted powders. Considering chemical SPTs, CM efficiently eliminates most surface anomalies while some irregular valleys remain, showing a limited capacity to fully modify surface characteristics. Similarly, CMP results in a more modified surface than CM, although some small micro-notches and surface waviness remained. In contrast, DE and ECP significantly minimize surface valleys, resulting in smoother and shinier surfaces. At increased magnification (Figure (c)), the DE configuration exhibits some remained dried slurry from the electrolytes on the surface. Also, the ECP treated surface shows a distinctive etched microstructure with interwoven patterns, indicating preferential electrochemical material removal at the grain boundaries as weaker regions of material which were more affected by corrosion than grains. Regarding the mechanical SPTs, AFM and M produce the most uniform surface conditions, with no surface anomalies. These surfaces have shallow, directional polishing or machining marks and minimal remained roughness/waviness. It can be seen that while all SPTs significantly modify the surface conditions, their success in enhancing surface morphology is highly reliant on the nature of each treatment.

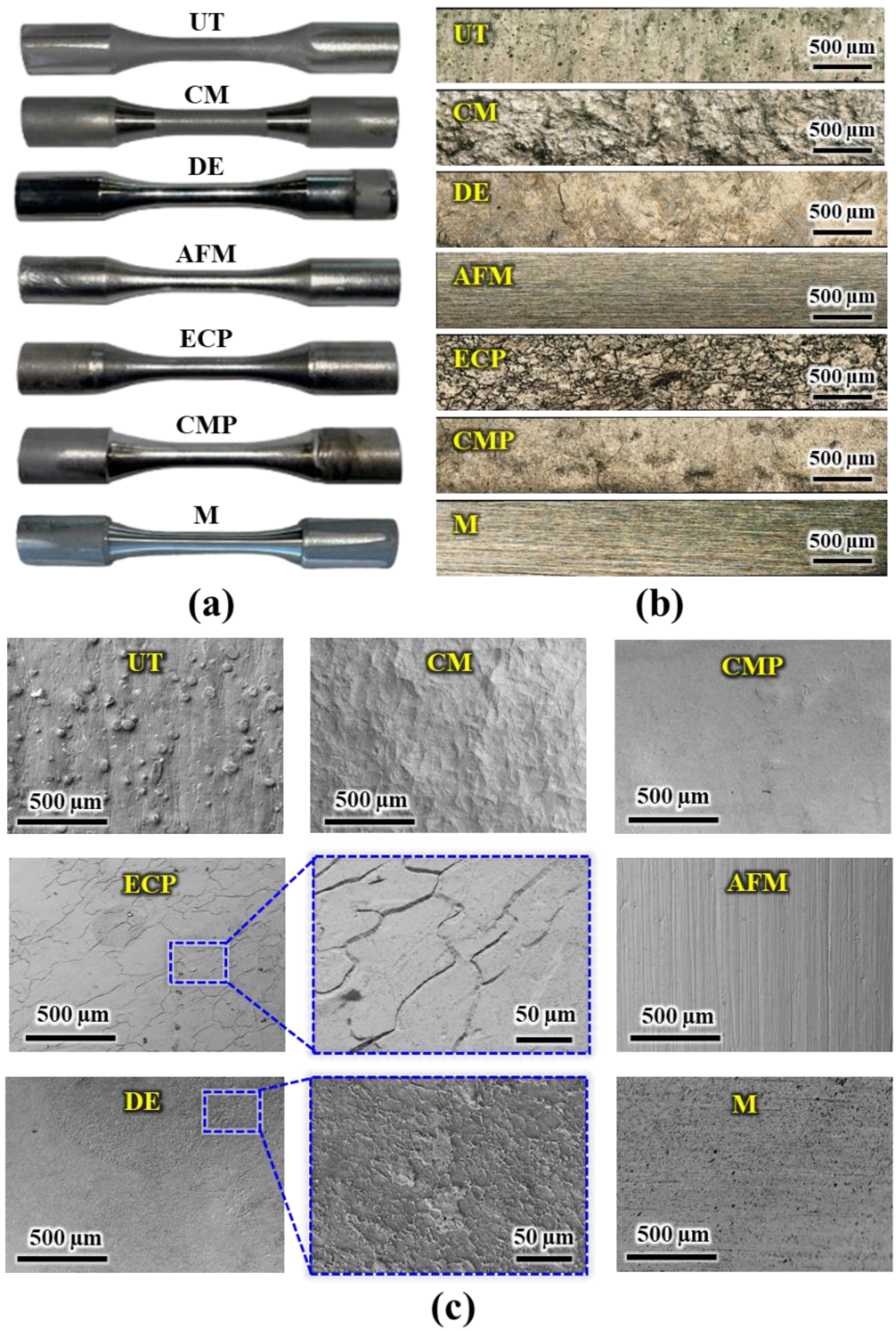

Figure 3. (a) Surface appearance of the specimens taken with camera, as well as surface textures in all conditions at different magnifications captured by (b) optical microscope and (c) SEM.

The 3D surface topography maps together with the corresponding areal surface roughness parameter values for all conditions are illustrated in **Error! Reference source not found.**. The surface height maps over 2 × 2 mm^2 areas as shown in **Error! Reference source not found.**(a), reveal pronounced differences in surface morphology depending on the applied treatment. The UT specimen shows high densities of peaks (due to presence of unmelted and partially melted feedstock) and deep valleys, indicating a high amount of surface anomalies associated with the as-built state; while, modified morphologies are observed after applying SPTs. After applying CM and CMP, most of the peaks were removed and some localized valleys remained reflected by moderated red distributions. In DE configuration, residual surface waviness still can be seen. Nonetheless, ECP, AFM, and M produce comparatively flattened and uniform surfaces with negligible height variation, indicating successful surface augmentation.

The quantitative examination of areal surface roughness characteristics further elaborates these observations as presented in **Error! Reference source not found.**(b) – (g). The UT specimen exhibits the highest roughness values among all height parameters with $S_a \approx 4.5$ µm, $S_v \approx 27.9$ µm, $S_p \approx 43.6$ µm, and $S_z \approx 70.3$ µm, indicating the presence of pronounced surface anomalies during the L-PBF process. On the other hand, applying SPTs leads to a considerable reduction in all roughness parameters. CM, CMP, and DE conditions show a decrease in all roughness metrics with $S_a \approx 1.5$–2 µm, $S_v \approx 7.5$–8.5 µm, $S_p \approx 9$–13 µm, and $S_z \approx 17$–21 µm, indicating acceptable smoothing of surface roughness. AFM, M, and ECP showed the most significant surface roughness modification respectively, achieving S_a values of approximately 0.4–0.7 µm and S_v, S_p, and S_z values in the ranges of 2–3 µm (only ECP showed higher S_v value around 7 µm), 3–6 µm, and 5–10 µm, respectively. In addition to height-based roughness parameters, similar trends were also observed for functional surface parameters of S_k and S_{vk}. CM, CMP, and DE conditions exhibit relatively higher S_k and S_{vk} values, attributed to the presence of some remaining valleys and waviness as well as localized chemical etching effects. In contrast, ECP, M, and AFM treated specimens show considerably lower S_k and S_{vk} values, indicating effective removal of both core roughness, peaks and valleys, and surface waviness. Considering roughness measurement results, as depicted in Figure 4(h), it can be seen that AFM had the highest influence for surface texture enhancement followed by M, ECP, CMP, CM, and DE respectively.

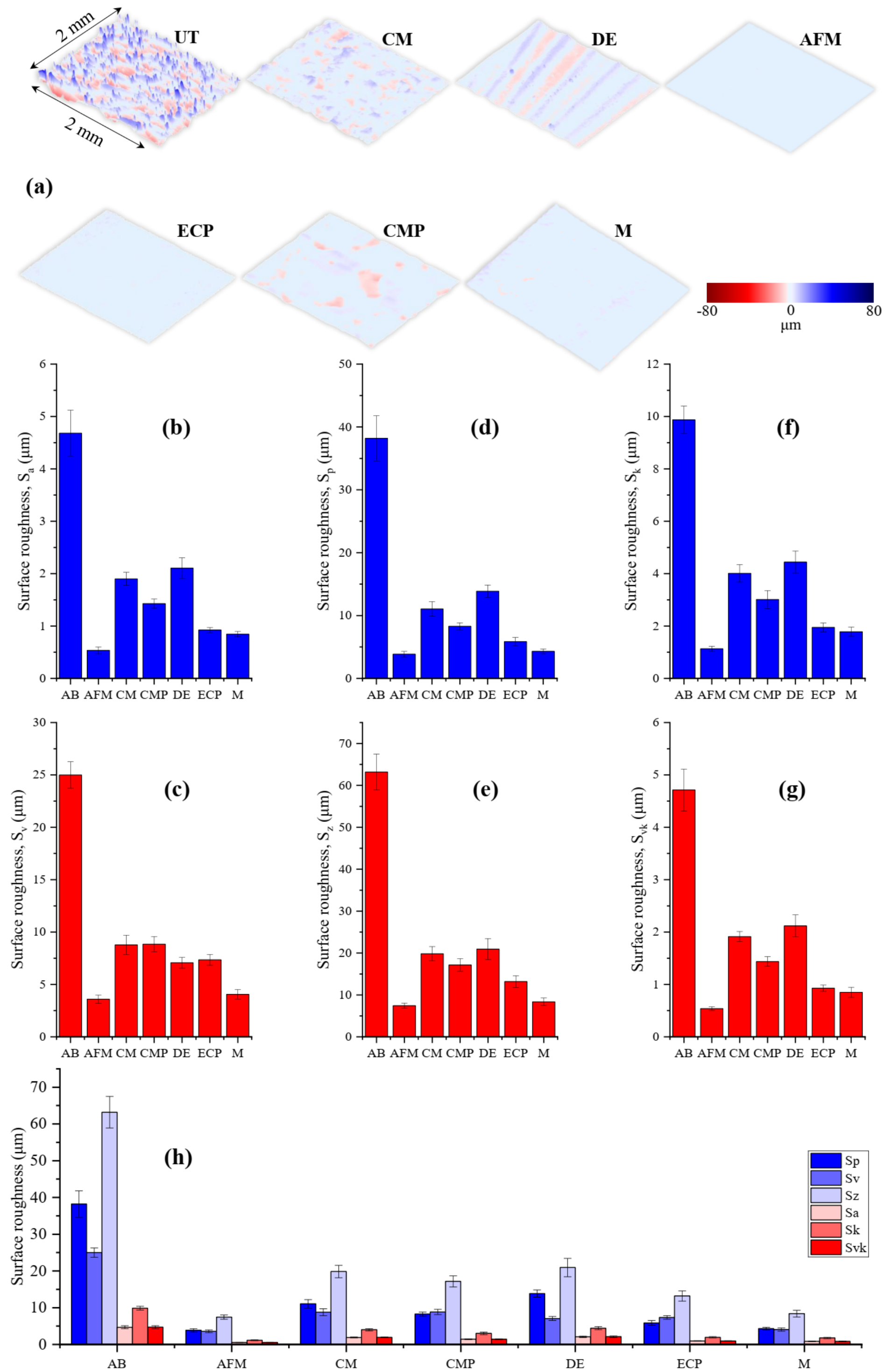

Figure 4. (a) 3D surface topography maps of all conditions obtained within a 2 × 2 mm² area. Surface roughness values in terms of (b) S_a, (c) S_v, (d) S_p, (e) S_z, (f) S_k and (g) S_{vk} parameters for all sets. (h) Comparison of efficiency of applied SPTs for surface texture modification compared to the as-built surface considering all roughness parameters.

3.2 Microstructure

Near-surface microstructural characterization for all conditions was carried out by EBSD-obtained inverse pole figure (IPF) and kernel average misorientation (KAM) maps as illustrated in 5. The EBSD scans were acquired from the radial plane, i.e., perpendicular to the build direction, covering an area of approximately 230 × 200 μm^2 underneath the top surface layer. No specific microstructural changes such as grain refinement were observed compared to the UT specimen in both IPF and KAM maps. The microstructure of UT and chemically treated conditions, including CM, DE, and ECP, exhibit well-defined and equiaxed grain structures with sharp grain boundaries in the IPF maps. Correspondingly, the KAM maps for these conditions show uniformly low misorientation values across the analyzed depth, indicating negligible accumulation of dislocations and confirming that these treatments preserve the heat-treated grain structure with minimal plastic deformation. However, the corresponding IPF maps of mechanically assisted SPTs of AFM, M, and CMP, display minor grain distortion limited to the shallow surface layer, with the underneath microstructure remaining largely unaffected. These sets show slightly elevated KAM values localized at the immediate treated surface. The KAM maps reveal high misorientation concentrated within the top ~5–10 µm, followed by a rapid reduction in KAM values with increasing depth. These elevated KAM values indicate localized plastic deformation due to surface-to-surface mechanical contacts of a material removal tool (in M) or particles (in AFM and CMP) to the specimen's surface.

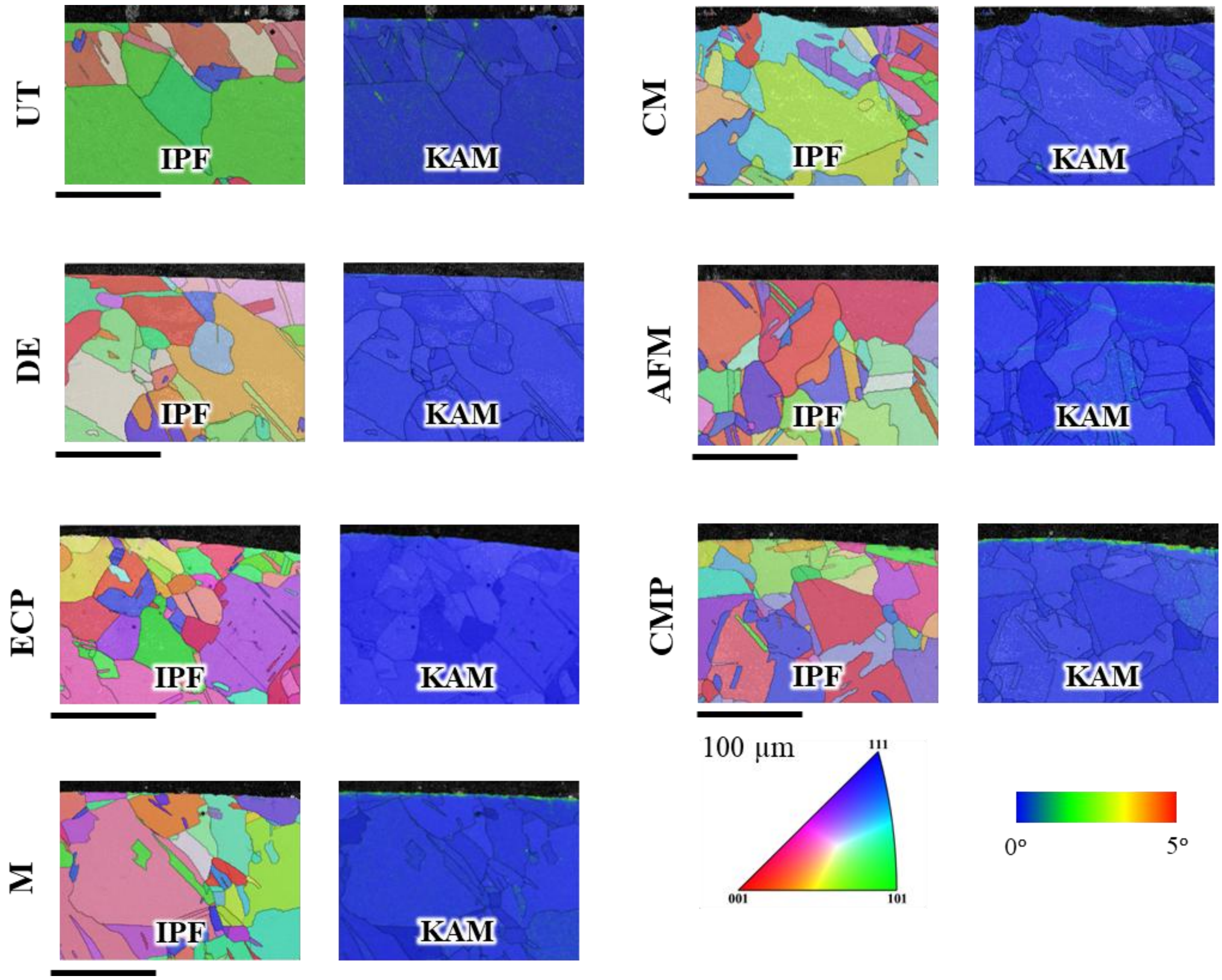

Figure 5. IPF and Kam maps of the microstructural characterization results obtained from EBSD for all conditions.

3.3 Fatigue Behavior

The fatigue testing laboratory reported some challenges during testing. It was reported that the temperature of the specimens rose (reaching approximately 40-60 ^{o}C in certain cases) under strain-control conditions during testing at the initially considered frequency of 10 Hz. This was particularly noted at strain amplitudes of ε_a = 0.003-0.005 mm/mm, prompting the use of lower frequencies to mitigate any temperature variations. Following a series of trials at frequencies of 5, 3, and 1 Hz, the laboratory conducted fatigue tests on specimens to confirm that no temperature increase occurred during testing. It should be noted that while the temperature increased to approximately 30-40 ^{o}C for ε_a = 0.0025 mm/mm, a loading frequency of 0.5 and 1 Hz was employed. Furthermore, for the fatigue tests initiated at low strain amplitudes (0.0025 and 0.003 mm/mm), after several hundred cycles, the force value was documented. Using this value, force-controlled fatigue tests were performed. In addition, for the specimens treated with AFM, as the standardized dog bone geometry was modified in the AFM processing to an hourglass-shaped gage, attachment of an extensometer was very challenging (and impossible in some specimens). As a result, the stress experienced by the machined specimens during testing at the lower strain amplitudes of 0.003 and 0.0025 mm/mm were designated to calculate the stress amplitudes for testing the AFM specimens.

The obtained strain-life (ε-N) results for all conditions are represented in Figure . The summary of fatigue test results is also represented in Appendix . It is important to highlight that all data presented is directly from the testing laboratory's reports. The observed inconsistency, especially for ε_a = 0.0025 and 0.003 mm/mm, can be attributed to testing issues and challenges employing different loading frequencies as well as possible temperature changes during testing. Figure (a) depicts the overall distribution of reversals to failure ($2N_f$) versus applied strain amplitudes and Figure (b)–5(e) indicate the fatigue life at different strain amplitudes of ε_a = 0.0025, 0.003, 0.004, and 0.005 mm/mm, separately.

At the lowest strain amplitude (ε_a = 0.0025 mm/mm), in which the elastic strain regime is dominant, the fatigue behavior shows strong dependency to the surface condition. The UT specimens exhibit the shortest fatigue lives which can be attributed due to the presence of highest surface roughness; particularly deep surface micro-notches that act as stress concentration zones and potential crack initiation sites. DE condition shows comparable fatigue lives to UT with slight life improvement only for one of the specimens. It should be noted that among all applied SPTs, DE had the least effect on surface roughness reduction. CM provided only limited improvement, while CMP and ECP result in relatively improved fatigue lives as surface irregularities and roughness were more reduced (compared to the DE). The highest fatigue lives at this strain level are achieved by mechanical SPTs of AFM and M conditions with lowest surface roughness values, which can be attributed to their superior surface planarization capability that effectively removes surface asperities and micro-notches acting as fatigue crack initiation sites. Thus indicating one to two orders of magnitude improvement compared to UT specimens, demonstrating the critical role of surface finish under elastic-dominated loading.

At an intermediate strain amplitude of ε_a = 0.003 mm/mm (Figure (c)), the beneficial effects of surface texture modification by applied SPTs remains evident but becomes less pronounced. While M, AFM, and ECP specimens still show higher fatigue lives. In this moderate strain level, the reduction in sensitivity to surface roughness is attributed to the increased contribution of plastic strain to the overall deformation, which decreases the dominance of surface-controlled crack initiation mechanisms.

As the strain amplitude increases further to ε_a = 0.004 mm/mm (Figure (d)) the fatigue lives of all conditions converge more closely; while ECP and M still exhibit slightly higher fatigue performance in comparison with other conditions. At this strain level, fatigue damage is governed mainly by cyclic plastic deformation within the material bulk, promoting rapid crack imitation independent of surface texture.

At the highest strain amplitude of ε_a = 0.005 mm/mm (Figure (e)), corresponding to a fully plastic strain regime, minimal differences in fatigue life can be observed among the various SPTs. The fatigue response is dominated by severe cyclic plasticity, leading to accelerated microcrack formation and propagation within the bulk material rather than at surface defects. Under these conditions, even specimens with highly refined surfaces (e.g., ECP and M) do not exhibit significant life improvement compared to the conditions with higher surface roughness values, as the crack initiation process is no longer surface-driven and its mostly influenced by bulk microstructural response which in this study the applied treatments did not show significant changes.

Overall, the influence of surface texture modification is masked by dominancy of the cyclic plastic regime in high strain amplitudes while the effects of surface condition are more pronounced under elastic or near-elastic strain conditions, where crack initiation can be highly affected by surface quality. The difference in the elastic and plastic regimes in the corresponding strain amplitudes can also be seen in hysteresis loops diagrams shown in Appendix . At the lower strain amplitudes (0.25% and 0.30%), the hysteresis loops indicate predominantly elastic deformation with limited energy dissipation per cycle. As the strain amplitude increases up to

0.40% and 0.50%, a noticeable widening of the hysteresis loops is observed, reflecting extensive plastic strain accumulation and elevated cyclic energy dissipation.

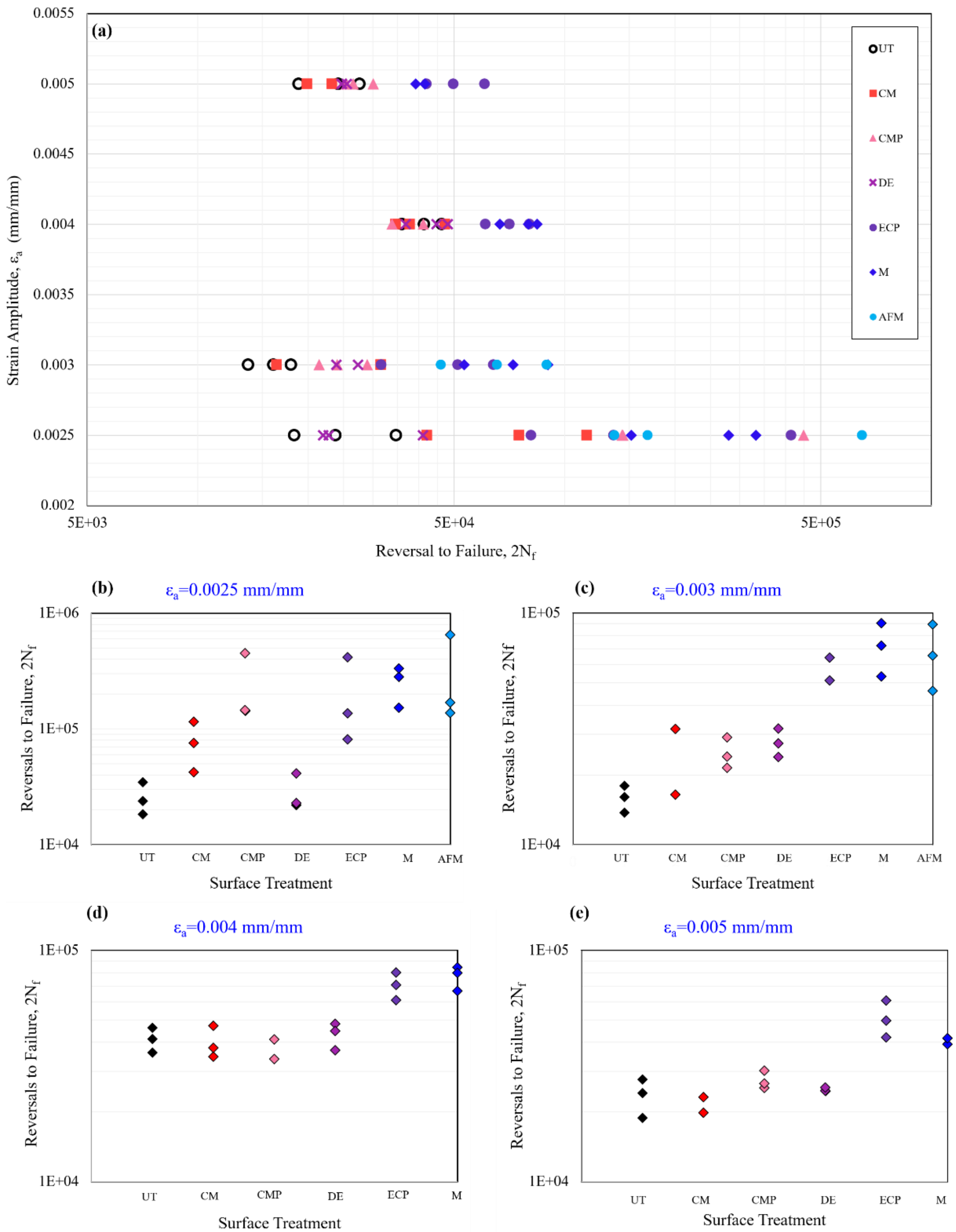

Figure 6. The results of strain-life fatigue tests for all conditions at (a) four different strain amplitudes and separately for strain amplitudes of (b) 0.0025 mm/mm, (c) 0.003 mm/mm, (d) 0.004 mm/mm, and (f) 0.005 mm/mm.

Fractographs of L-PBF Alloy 214 specimens for all conditions are shown in Figure . Figure (a) presents representative low and high magnification SEM images of the fracture surfaces for failed specimens at ε_a = 0.0025 mm/mm. For all conditions, the fracture surfaces exhibited dominancy of surface crack initiations. As indicated by red arrows, fatigue crack initiation is observed at or near the surface of the specimens, confirming the surface-controlled nature of fatigue failure under the applied loading condition. Considering high strain amplitudes of ε_a = 0.004 and 0.005 mm/mm (shown in Figure (b)), the pattern of fatigue failure due to the presence of plastic regime was changed and turned to relatively brittle fracture. Multiple surface crack sites with almost no clear dominant river marks as location of main crack initiation, especially at ε_a = 0.005 mm/mm (compared to the ones at ε_a = 0.0025 mm/mm) can be seen. In addition, remaining surface valleys after insufficient surface material removal by CM are shown by green arrows. It can be seen that due to high plastic strains, these surface valleys were elongated following the loading direction.

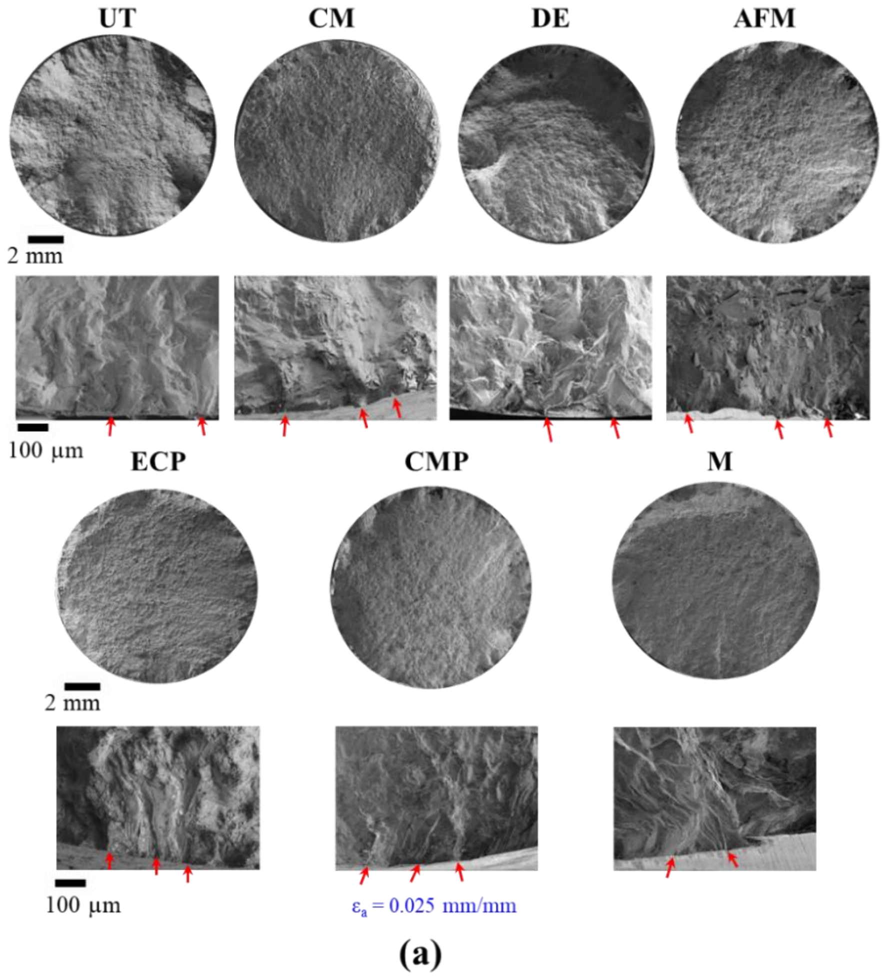

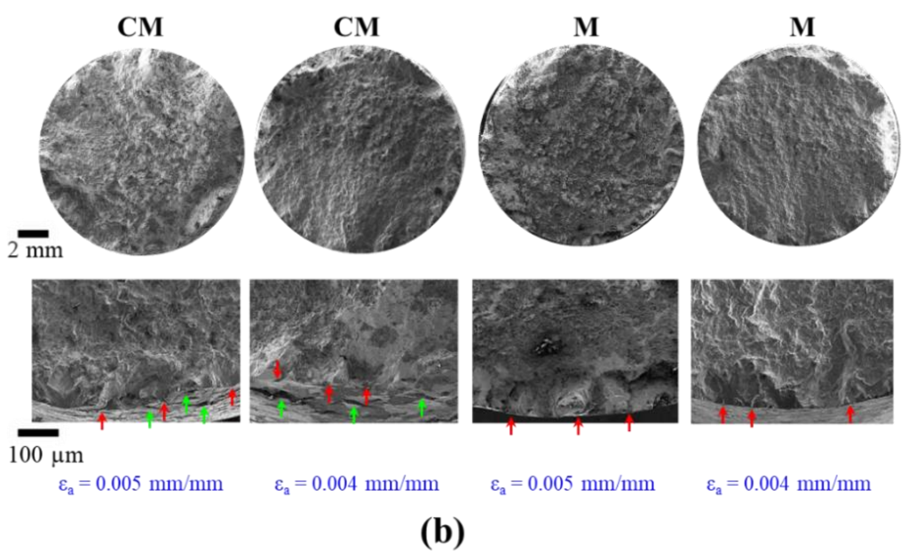

Figure 7. SEM fracture surfaces of failed specimens tested at strain amplitude of (a) $\varepsilon_a = 0.0025$ mm/mm and (b) $\varepsilon_a = 0.004$ and 0.005 mm/mm. In addition, red and green arrows demonstrate surface crack initiation and remained surface valleys, respectively.

4.0 CONCLUSIONS

In this paper the effects of different surface post treatments (SPTs) on heated treated and HIP-ed L-PBF fabricated Alloy 214 specimens for investigating the surface texture enhancement and fatigue behavior improvement were studied. Six different SPTs including CM, DE, ECP, CMP, AFM, and M were applied on the specimens. According to the achieved results, the following conclusions can be drawn:

1. All of the applied SPTs modified the surface texture (compared to the as-built state) efficiently but with different surface finish due to the differences in the nature of treatments. After applying CM and CMP, some surface valleys remained on the surface, while other SPTs effectively removed the surface valleys. Surface roughness measurement results revealed that AFM had the highest effect for surface texture enhancement followed by M, ECP, CMP, CM, and DE respectively.

2. Overall, applied SPTs exhibit no effect of microstructural variations. Only treatments involved with mechanical contact including AFM, M, and CMP show slightly localized plastic deformation on the top surface with depth of ~5–10 µm.

3. Fatigue behavior improvement was more pronounced in the lowest strain amplitude of ε_a = 0.0025 mm/mm, in which the elastic strain regime was dominant, and the fatigue behavior was dependent on the surface condition.

4. In highest strain amplitude of ε_a = 0.005, fatigue lives of all conditions converged more closely, and the least improvement was obtained. In this strain amplitude, preliminary fatigue failure governed by plastic regime within the material bulk promot rapid crack imitation almost independent of surface condition.

5. Considering fatigue test results at all strain amplitudes, M, AFM, and ECP showed the highest effects on fatigue behavior improvement respectively. Also, CM, CMP, and DE mostly show very low or moderate fatigue life enhancement.

Appendix A

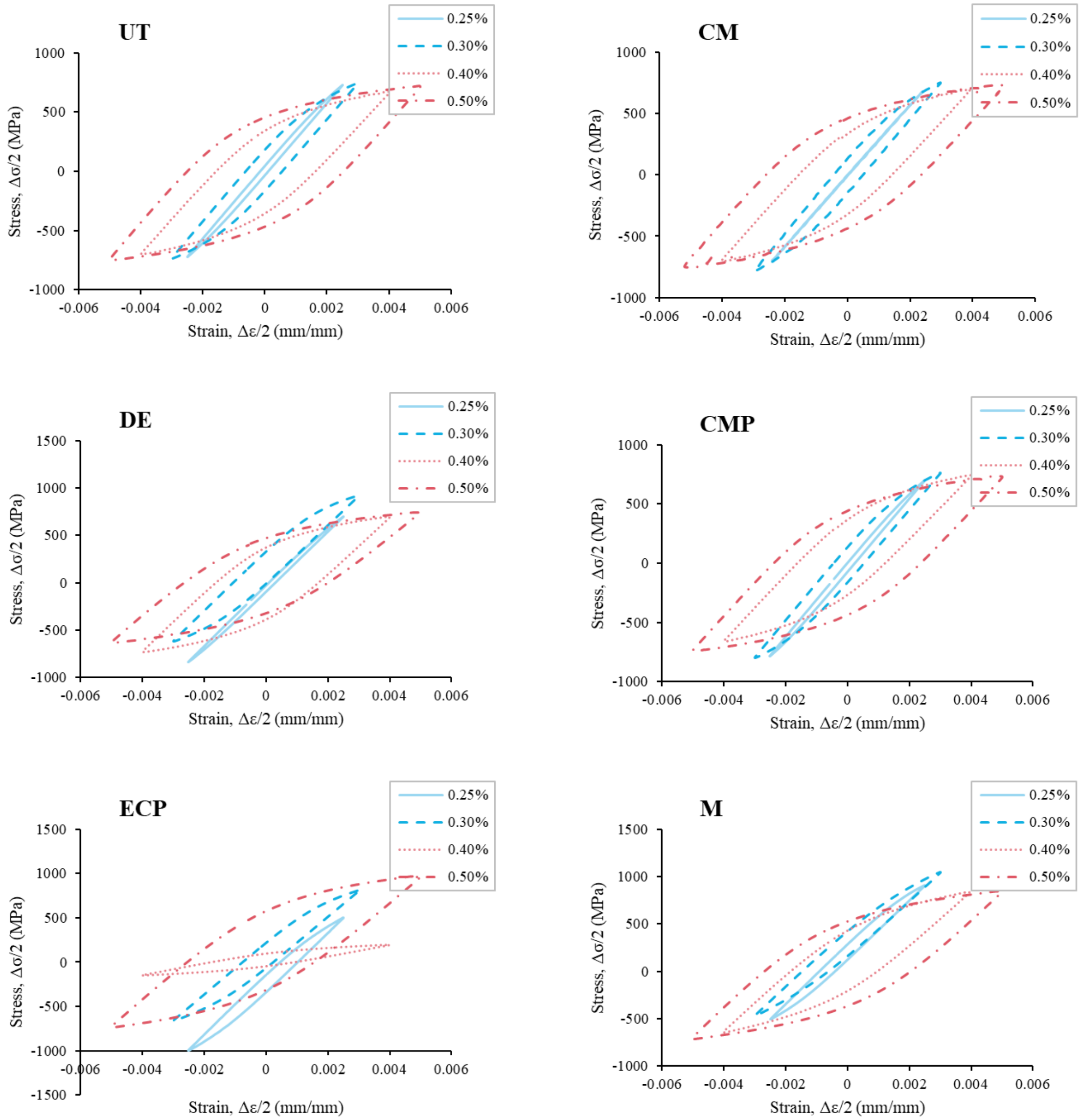

Figure 3. The hysteresis loops corresponding to different strain amplitudes demonstrating elastic and plastic regimes in the untreated and treated conditions.

Appendix B

Table 2. A summary of strain-life fatigue results for various surface conditions at $R_\varepsilon = -1$.

Condition	Specimen	Cross-section area	ε_a (mm/mm)	$\Delta\varepsilon_e/2$ (mm/mm)	$\Delta\varepsilon_p/2$ (mm/mm)	σ_a (MPa)	$2N_f$
UT	B6	31.014	0.003	0.002	0.000	512.752	18346
	B9	31.014	0.003	0.002	0.000	498.242	23776
	B2	30.851	0.003	0.002	0.000	485.907	34750
	B18	31.014	0.003	0.002	0.001	508.020	16064
	B14	30.901	0.003	0.003	0.000	505.907	13740
	B4	30.914	0.003	0.002	0.001	512.492	17952
	B15	30.801	0.004	0.002	0.002	474.606	41400
	B3	30.739	0.004	0.002	0.002	483.182	36068
	B12	30.801	0.004	0.002	0.002	479.570	46220
	B16	30.926	0.005	0.003	0.002	500.906	18860
	B1	30.739	0.005	0.003	0.002	495.440	27612
	B5	31.001	0.005	0.003	0.002	504.898	24152
CM	P110	34.043	0.003	0.002	0.000	472.698	75148
	P106	32.459	0.003	0.003	0.000	527.717	31530
	P83	32.434	0.004	0.002	0.002	504.354	34596
	P69	32.434	0.004	0.003	0.001	481.198	47184
	P35	33.208	0.004	0.002	0.002	492.661	37866
	P46	32.820	0.005	0.003	0.002	511.054	23192
	P86	32.949	0.005	0.002	0.003	504.357	19842
DE	P72	38.599	0.003	0.002	0.003	529.992	21948
	P1	38.879	0.003	0.002	0.003	504.014	22746
	P26	38.879	0.003	0.002	0.003	497.845	41124
	P38	38.879	0.003	0.002	0.003	532.873	23840
	P96	38.320	0.003	0.002	0.003	530.524	27316
	P65	39.301	0.004	0.002	0.004	479.509	36872
	P27	39.443	0.004	0.002	0.004	501.187	48090
	P75	39.160	0.004	0.002	0.004	494.497	44740
	P89	40.124	0.005	0.003	0.005	512.457	24724
	P40	39.697	0.005	0.003	0.005	511.418	24668
ECP	P42	32.140	0.003	0.002	0.003	497.483	40536
	P32	32.395	0.003	0.002	0.003	485.400	207292
	P22	30.989	0.003	0.002	0.002	491.863	67984
	P87	31.644	0.003	0.002	0.003	514.780	15828
	P73	31.631	0.003	0.002	0.003	517.960	25552
	P100	31.555	0.003	0.002	0.003	512.880	31988

	P2	31.606	0.004	0.003	0.004	510.431	30456
	P105	31.695	0.004	0.003	0.004	498.442	35358
	P51	32.089	0.004	0.003	0.004	496.946	40086
	P62	30.914	0.005	0.003	0.005	546.070	20996
CMP	P59	30.539	0.003	0.002	0.003	484.226	144268
	P70	31.165	0.003	0.002	0.003	510.485	143332
	P102	30.664	0.003	0.002	0.002	514.432	448368
	P3	31.165	0.003	0.002	0.003	518.675	21432
	P76	30.539	0.003	0.003	0.003	539.982	23964
	P23	31.039	0.003	0.002	0.003	525.617	28944
	P93	31.240	0.004	0.002	0.004	501.441	33818
	P50	31.416	0.004	0.003	0.004	484.374	41156
	P36	30.914	0.005	0.003	0.005	512.561	25394
	P98	30.539	0.005	0.003	0.005	521.048	30084
	P104	30.789	0.005	0.003	0.005	512.010	26498
M	P99	31.290	0.003	0.002	0.000	492.662	140006
	P13	31.669	0.003	0.002	0.000	488.106	76064
	P12	31.454	0.003	0.002	0.000	492.134	166334
	P63	31.429	0.003	0.002	0.001	515.750	36160
	P21	31.454	0.003	0.003	0.000	526.950	45062
	P55	31.429	0.003	0.003	0.000	556.740	26602
	P28	31.442	0.004	0.002	0.002	495.699	42100
	P82	31.517	0.004	0.002	0.002	500.350	39810
	P4	31.265	0.004	0.003	0.001	504.315	33342
	P58	31.429	0.005	0.003	0.002	539.610	19630
	P24	31.695	0.005	0.003	0.002	534.177	20816

REFERENCES

[1] Maleki, E., Unal, O., Guagliano, M. & Bagherifard, S. The effects of shot peening, laser shock peening and ultrasonic nanocrystal surface modification on the fatigue strength of Inconel 718. Mater. Sci. Eng. A (2021) doi:10.1016/j.msea.2021.141029.

[2] Volpato, G. M., Tetzlaff, U. & Fredel, M. C. A comprehensive literature review on laser powder bed fusion of Inconel superalloys. Additive Manufacturing at https://doi.org/10.1016/j.addma.2022.102871 (2022).

[3] Gradl, P. R. et al. Geometric feature reproducibility for laser powder bed fusion (L-PBF) additive manufacturing with Inconel 718. Addit. Manuf. (2021) doi:10.1016/j.addma.2021.102305.

[4] Katsarelis, C. et al. Additive Manufacturing of NASA HR-1 Material for Liquid Rocket Engine Component Applications. JANNAF Dec (2019).

[5] Gradl, P. et al. Advancement of extreme environment additively manufactured alloys for next generation space propulsion applications. Acta Astronaut. (2023) doi:10.1016/j.actaastro.2023.06.035.

[6] Maleki, E. et al. Introducing gradient severe shot peening as a novel mechanical surface treatment. Sci. Rep. (2021) doi:10.1038/s41598-021-01152-2.

[7] June, D., Pourjam, M., Gradl, P., Demeneghi, G. & Hazeli, K. High-temperature behavior of additively manufactured Haynes 214: Ductility loss and deformation mechanisms transition. Addit. Manuf. 97, 104600 (2025).

[8] Liu, J. et al. Microstructure evolution and work hardening behaviour during cold deformation of Haynes 214 superalloy. J. Mater. Res. Technol. (2023) doi:10.1016/j.jmrt.2023.04.194.

[9] Ulan kyzy, S. et al. Thermo-physical properties of Hastelloy X and Haynes 214 close to the melting range. Materials Science and Technology (United Kingdom) at https://doi.org/10.1080/02670836.2020.1753154 (2020).

[10] Wang, Y., Liu, Y., Tang, H. & Li, W. Oxidation behaviors of porous Haynes 214 alloy at high temperatures. Mater. Charact. (2015) doi:10.1016/j.matchar.2015.07.026.

[11] Keleshteri, M. M., Pourjam, M., Mayeur, J. R. & Hazeli, K. Temperature-dependent mechanical properties and crystal plasticity parameters for additively manufactured Haynes-214 alloy: Experiments and numerical modeling. Addit. Manuf. (2024) doi:10.1016/j.addma.2024.104499.

[12] Ganesan, P., Smith, G. D. & Yates, D. H. Performance of inconel alloy 617 in actual and simulated gas turbine environments. Mater. Manuf. Process. (1995) doi:10.1080/10426919508935080.

[13] McIlroy, K., Zawierucha, R. & Million, J. F. Promoted ignition-combustion behavior of alternative high performance engineering alloys in oxygen-enriched atmospheres. ASTM Spec. Tech. Publ. (1997) doi:10.1520/stp12052s.

[14] Winner, J. D. & Morehart, J. H. Particle-Impact Ignition Testing of Three Commercially Available Ignition Resistant Metal Alloys. in AIAA SciTech Forum and Exposition, 2023 (2023). doi:10.2514/6.2023-1490.

[15] Hattali, M. L., Valette, S., Ropital, F., Mesrati, N. & Tréheux, D. Interfacial behavior on Al 2O 3/HAYNES ® 214TM joints fabricated by solid state bonding technique with Ni or Cu-Ni-Cu interlayers. J. Eur. Ceram. Soc. (2012) doi:10.1016/j.jeurceramsoc.2012.01.036.

[16] Mostafaei, A. et al. Additive manufacturing of nickel-based superalloys: A state-of-the-art review on process-structure-defect-property relationship. Progress in Materials Science at https://doi.org/10.1016/j.pmatsci.2023.101108 (2023).

[17] Zhu, G. et al. Advances in additive manufacturing of nickel-based high-temperature alloys. Cailiao Gongcheng/Journal of Materials Engineering at https://doi.org/10.11868/j.issn.1001-4381.2023.000676 (2024).

[18] Hu, Y. et al. Laser additive manufacturing of nickel-based superalloys: A review. Materials Science in Additive Manufacturing at https://doi.org/10.36922/MSAM025240051 (2026).

[19] Son, K. T. et al. The creep and fracture properties of additively manufactured inconel 625. Materialia (2021) doi:10.1016/j.mtla.2021.101021.

[20] Graybill, B. et al. Additive manufacturing of nickel-based superalloys. in ASME 2018 13th International Manufacturing Science and Engineering Conference, MSEC 2018 (2018). doi:10.1115/MSEC2018-6666.

[21] Maleki, E., Bidar, A., Rahmdel, K., Shao, S. & Shamsaei, N. Laser beam powder bed fused AlSi10Mg: An overview on the effect of post-processing on the microstructure and mechanical properties. Mater. Des. (2026) doi:10.1016/j.matdes.2025.115336.

[22] Maleki, E., Salehnasab, B., Paul, M., Shao, S. & Shamsaei, N. Dimensional accuracy of fabricated geometries through powder bed fusion: An overview and a new benchmark artifact proposal. Mater. Des. 257, 114361 (2025).

[23] Ahmad, N. et al. Determining critical surface features affecting fatigue behavior of additively manufactured Ti-6Al-4V. Int. J. Fatigue 197, 108956 (2025).

[24] Maleki, E., Bagherifard, S. & Guagliano, M. Application of artificial intelligence to optimize the process parameters effects on tensile properties of Ti-6Al-4V fabricated by laser powder-bed fusion. Int. J. Mech. Mater. Des. (2022) doi:10.1007/s10999-021-09570-w.

[25] Maleki, E., Bagherifard, S., Unal, O. & Guagliano, M. Hybrid Intelligence approach to study post-processing impact on the mechanical performance of notched additively manufactured AlSi10Mg. Mater. Des. 248, 113462 (2024).

[26] Maleki, E., Bagherifard, S., Unal, O., Bandini, M. & Guagliano, M. On the effects of laser shock peening on fatigue behavior of V-notched AlSi10Mg manufactured by laser powder bed fusion. Int. J. Fatigue (2022) doi:10.1016/j.ijfatigue.2022.107035.

[27] May, P. E. et al. Influence of heat treatment on the high temperature properties of Inconel 718 fabricated via Laser Beam Powder Bed Fusion. J. Mater. Res. Technol. 36, 9881–9897 (2025).

[28] Cavalcante, T. R. F. et al. Microstructural assessment of additive-manufactured Inconel 718 samples subjected to heat treatments for enhanced mechanical properties. Prog. Addit. Manuf. (2025) doi:10.1007/s40964-025-01279-y.

[29] Taller, S. & Austin, T. Using post-processing heat treatments to elucidate precipitate strengthening of additively manufactured superalloy 718. Addit. Manuf. (2022) doi:10.1016/j.addma.2022.103280.

[30] Kim, K. S., Kang, T. H., Kassner, M. E., Son, K. T. & Lee, K. A. High-temperature tensile and high cycle fatigue properties of inconel 625 alloy manufactured by laser powder bed fusion. Addit. Manuf. (2020) doi:10.1016/j.addma.2020.101377.

[31] Marchese, G. et al. Heat-Treated Inconel 625 by Laser Powder Bed Fusion: Microstructure, Tensile Properties, and Residual Stress Evolution. J. Mater. Eng. Perform. (2024) doi:10.1007/s11665-024-09235-7.

[32] Li, K. et al. Effect of solid-solution treatment on high-temperature properties and creep fracture mechanism of laser powder bed fused Inconel 625 alloy. Mater. Sci. Eng. A 902, 146592 (2024).

[33] Boswell, J. et al. The effects of energy density and heat treatment on the microstructure and mechanical properties of laser additive manufactured Haynes 282. Mater. Des. (2021) doi:10.1016/j.matdes.2021.109725.

[34] Shaikh, A. S., Schulz, F., Minet-Lallemand, K. & Hryha, E. Microstructure and mechanical properties of Haynes 282 superalloy produced by laser powder bed fusion. Mater. Today Commun. (2021) doi:10.1016/j.mtcomm.2021.102038.

[35] Ahmad, N., Ghiaasiaan, R., Gradl, P. R., Shao, S. & Shamsaei, N. Low cycle fatigue behavior of additively manufactured Haynes 282: Effect of post-processing and test temperature. Int. J. Fatigue (2023) doi:10.1016/j.ijfatigue.2023.107880.

[36] Baig, S., Gradl, P. R., Shao, S. & Shamsaei, N. Temperature dependent tensile behavior of additively manufactured HAYNES® 214: A comparative study between laser powder bed fusion and laser powder directed energy deposition. J. Mater. Res. Technol. 32, 1683–1695 (2024).

[37] Holmberg, J. et al. Machining of additively manufactured alloy 718 in as-built and heat-treated condition: surface integrity and cutting tool wear. Int. J. Adv. Manuf. Technol. (2024) doi:10.1007/s00170-023-12727-w.

[38] Kaynak, Y. & Tascioglu, E. Post-processing effects on the surface characteristics of Inconel 718 alloy fabricated by selective laser melting additive manufacturing. Prog. Addit. Manuf. (2020) doi:10.1007/s40964-019-00099-1.

[39] Lee, S. et al. Fatigue behavior and modeling of additively manufactured IN718: The effect of surface treatments and surface measurement techniques. J. Mater. Process. Technol. (2022) doi:10.1016/j.jmatprotec.2021.117475.

[40] Jiang, D., Tian, Y., Zhu, Y. & Huang, A. Investigation of surface roughness post-processing of additively manufactured nickel-based superalloy Hastelloy X using electropolishing. Surf. Coatings Technol. (2022) doi:10.1016/j.surfcoat.2022.128529.

[41] Rapid Analysis and Manufacturing Propulsion Technology (RAMPT)- NASA. Marshall Space Flight Center https://www.nasa.gov/rapid-analysis-and-manufacturing-propulsion-technology/ (2024).

[42] ASTM INTERNATIONAL. ASTM E606 –Standard Practice for Strain-Controlled Fatigue Testing. 01, (1998).

[43] Baig, S., Gradl, P. R., Shao, S. & Shamsaei, N. Temperature dependent tensile behavior of additively manufactured HAYNES® 214: A comparative study between laser powder bed fusion and laser powder directed energy deposition. J. Mater. Res. Technol. (2024) doi:10.1016/j.jmrt.2024.08.031.

[44] Wang, J. et al. Research Status and Prospect of Laser Scribing Process and Equipment for Chemical Milling Parts in Aviation and Aerospace. Micromachines at https://doi.org/10.3390/mi13020323 (2022).

[45] Bologna, O. et al. Investigating post-processing impact on fatigue performance of LPBF Ti6Al4V with heat treatment, high pressure heat treatment, and dry electropolishing strategies. Int. J. Fatigue (2024) doi:10.1016/j.ijfatigue.2024.108365.

[46] Maleki, E., Bagherifard, S., Sabouri, F., Bandini, M. & Guagliano, M. Hybrid thermal, mechanical and chemical surface post-treatments for improved fatigue behavior of laser powder bed fusion AlSi10Mg notched samples. Surf. Coatings Technol. (2022) doi:10.1016/j.surfcoat.2021.127962.

[47] Lee, H., Kim, H. & Jeong, H. Approaches to Sustainability in Chemical Mechanical Polishing (CMP): A Review. International Journal of Precision Engineering and Manufacturing - Green Technology at https://doi.org/10.1007/s40684-021-00406-8 (2022).

[48] Gradl, P., Cervone, A. & Colonna, P. Development and experimental evaluation of surface enhancement methods for laser powder directed energy deposition microchannels. Virtual Phys. Prototyp. 19, (2024).

[49] International Organization for Standardization. ISO 25178-2:2021 - Geometrical product specifications (GPS) — Surface texture: Area. Part 2: Terms, definitions and surface texture parameters (2021).